2026 IEEE International Conference on Robotics and Automation (ICRA 2026)
June 1-5, 2026. Vienna, Austria

A Parametric Wave-Structured 3-DoF Compliant Joint with Tunable Stiffness

Anjum Saeed[1,*], Mihai Dragusanu[1,*], Monica Malvezzi[1], Domenico Prattichizzo[1] and Gionata Salvietti[1]

***Abstract*— Soft–rigid tendon-driven robotic hands are widely adopted due to their simple fabrication and effective compliance, enabling robust and adaptive grasping. However, achieving dexterity, such as in-hand manipulation, remains challenging because actuation systems typically constrain finger trajectories. This paper presents a novel *parametric wave-structured 3-DoF compliant joint with tunable stiffness*, designed to enhance dexterity while maintaining a compact form factor. The joint combines a compliant structure and a particular geometry with a Twisted String Actuation (TSA) system, allowing simultaneous modulation of joint stiffness and the mobility of a universal joint that can be used to resemble flexion/extension and abduction/adduction motion of the human hand fingers. Two tendons, independently actuated, control asymmetric bending and stiffness regulation, while a third tendon drives flexion/extension. Analytical modeling and numerical simulations are provided to characterize the kinematics, statics, and stiffness modulation properties of the joint. A functional prototype demonstrates significant improvements in workspace and dexterity when integrated as the base joint of a wearable robotics supernumerary finger. Experimental evaluations validate the proposed design and confirm its potential as a versatile building block for dexterous, lightweight, and adaptive robotic hands.**

I. Introduction

Soft–rigid grippers are emerging as a promising class of soft robotic hands due to their ease of fabrication, enabled by rapid prototyping techniques, and their relatively simple control strategies, often based on tendon-driven actuation systems. Several examples of soft–rigid grippers are available in the literature, including open source solutions [1]–[3]. One of the key advantages of soft–rigid grippers is that their soft joints provide compliance, allowing the fingers to passively adapt to the shape of the grasped object. As a result, stable grasps can be achieved through simple flexion of the fingers.

However, achieving dexterity, such as performing in-hand manipulation, remains a significant challenge for tendon-driven hands. Modifying finger trajectories solely through control is difficult because tendon routing often constrains the motion to predefined paths. One possible solution is to design the stiffness of the soft joints to achieve different flexion trajectories, thereby enabling more advanced manipulation capabilities [4]. The approach consists in computing the stiffness of the single joint necessary to obtain a certain trajectory once the tendon is pulled to achieve finger flexion. The desired stiffness is then obtained by regulating the infill density parameter during the 3D printing of the joint. This approach requires physically replacing the joints, which cannot be done during operation, and restricts the design to a modular configuration. The literature on variable stiffness actuators (VSAs) offers numerous solutions, including designs implemented in robotic hands [5], [6], where stiffness modulation usually mimics the co-contraction capabilities of the human hand. Although effective, these designs are often fully actuated and involve a large number of control variables, leading to increased system complexity and challenging control strategies. More recently, Dragusanu *et al.* introduced a wave-shaped joint in [7], where stiffness can be modulated by compressing the entire joint structure using an additional tendon dedicated solely to stiffness regulation [8]. Similarly, Mansueto *et al.* [9] presented an optimization framework to map desired stiffness values to joint geometry parameters. However, these approaches rely on monolithic rigid joints designed to emulate compliant behavior. Moreover, these joints typically enable motion in a single bending direction, making them suitable for predefined flexion/extension trajectories, but limiting their ability to support more complex motion patterns.

In this paper, we present a novel *soft joint* architecture that combines stiffness modulation with enhanced motion capabilities, specifically enabling multi-degree-of-freedom (DoF) actuation for soft-rigid tendon driven robotic fingers. Inspired by the human metacarpophalangeal (MCP) joint, which allows both flexion/extension and abduction/adduction, the proposed joint integrates a compliant structure with tendon-driven actuation to achieve similar capabilities plus the possibility of changing the stiffness of the joint. Two tendons, independently actuated by separate motors, allow the joint to bend asymmetrically, thus reproducing abduction/adduction. When actuated simultaneously, these tendons compress the joint structure, modulating its bending stiffness as if tightening a nonlinear spring. A third tendon, driven by an additional motor, controls flexion/extension. To ensure a compact and efficient implementation, the joint uses a twisted string actuation (TSA) system, which provides high torque output while minimizing motor size and overall device footprint. The joint is fully characterized both analytically and ex-

We acknowledge the support of the European Union by the Next Generation EU project ECS00000017 “Ecosistema dell’Innovazione” Tuscany Health Ecosystem (THE, PNRR: Spoke 9 - Robotics and Automation for Health), and by the Horizon Europe project “HARIA - Human-Robot Sensorimotor Augmentation - Wearable Sensorimotor Interfaces and Supernumerary Robotic Limbs for Humans with Upper-limb Disabilities” (GA No. 101070292) and Italian Ministry of Research, under the complementary actions to the NRRP “Fit4MedRob - Fit for Medical Robotics” Grant (PNC0000007, CUP B53C22006960001).

[1]are with the Department of Information Engineering and Mathematics, University of Siena, Siena, Italy {saeed, malvezzi, prattichizzo, salviettigio}@diism.unisi.it. Corresponding Author contact: mihai.dragusanu2@unisi.it.

*Contributed equally to this work.

perimentally, including derivation of its forward and inverse kinematics, as well as evaluation of its stiffness modulation capabilities. A functional prototype is integrated as the base joint of a wearable supernumerary robotic finger that can be used to enhance grasping capabilities in subjects with an impaired hand motion [10], demonstrating a significant increase in workspace and dexterity compared to previous designs.

The remainder of this paper is organized as follows. Section II introduces the joint design, modeling, and TSA kinematic and static relationships, supported by numerical simulations. Section III presents the experimental setup and results of the joint characterization. Section IV describes its integration into a wearable robotic supernumerary finger, followed by conclusions in Section V.

II. Methodology

In this section, we present the parametric wave-structured 3-DoF compliant joint with tunable stiffness design and describe its behavior through joint modeling and numerical simulations.

A. Design

The proposed joint is characterized by a sinusoidal wave profile, whose geometry is defined by the following parameters: joint length (l_{th}), number of ridges (n_r), wave height (h_t), offset (off_t), and wave thickness (t_k). Among these, off_t and t_k enable modulation of the joint thickness along two orthogonal directions, thus allowing for tailored mechanical responses depending on the application requirements. This parametric design approach makes the joint highly versatile, as its stiffness and range of motion can be systematically adjusted.

An example of a wave-shaped compliant joint is presented in Fig. 1, with parameters $l_{th} = 22.5$ mm, $n_r = 2$, $h_t = 20$ mm, $off_t = 3$ mm, and $t_k = 8$ mm. The holes along the lateral sides of the wave structure are designed to route the TSA tendons. Two of the TSAs are threaded through these lateral passages, one of which is visible in the figure, and are responsible for controlling both the stiffness and the lateral motions of the joint. A third TSA is routed externally, passing outside the wave structure and through the rigid bodies, and is dedicated to controlling joint flexion. This integration of the tendon routing within the compliant structure ensures compactness facilitating direct coupling between the tendon actuation and the joint compliant deformation.

To investigate the tunability of stiffness, the present study focuses on varying l_{th} and t_k, as both parameters directly influence the mechanical response. Increasing l_{th} effectively enlarges the compliant region, thereby reducing stiffness, while increasing t_k enhances the joint's load-bearing capability, leading to higher stiffness. In contrast, off_t and h_t were kept constant, as was the distance between successive ridges, thus fixing the wave frequency. The experimental design therefore considers a family of joints defined by $l_{th} \in \{22.5, 30, 37.5, 45\}$ mm and $t_k \in \{8, 10, 12\}$ mm, allowing systematic evaluation of the effect of these parameters on joint behavior.

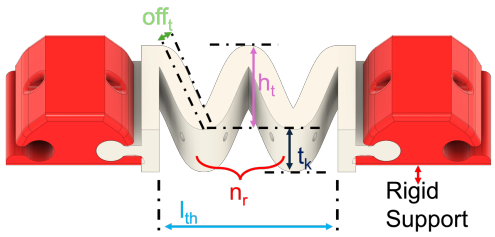

Fig. 1: Scheme of a the 3-DoF compliant joint, showing the parameters that can be varied in the design process.

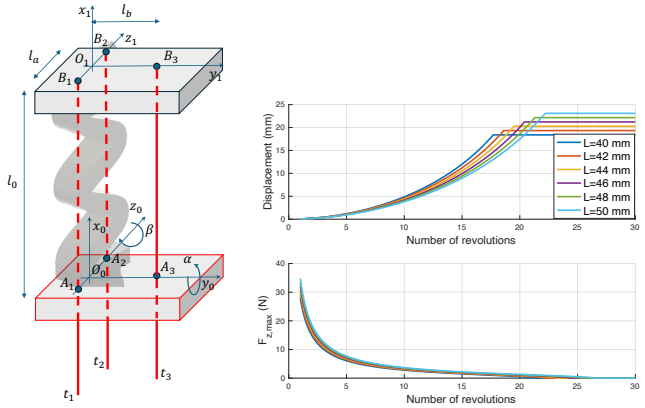

(a) (b)

Fig. 2: (a) Scheme of the 3-DoF compliant joint with the main model definitions. (b) TSA simulation: actuator displacement and maximum force as a function of actuation rotation angles for different values of the length l_0. Results are obtained with $r_s = 0.3$ mm, l_0 varying from 40 to 50 mm, and $\tau_t = 0.228$ Nm.

B. Joint model and kinematics analysis

In this subsection, we present the scheme and kinematic model of the proposed 3-DoF actuated joint and the main direct, inverse, and differential kinematics relationships.

In particular, we investigate the forward and inverse kinematic relationships between the actuator rotation angles and the joint configuration. The joint is 3-DoF, and three parameters are needed to represent it, specifically the angles α (joint adduction/abduction), β (joint flexion/extension) and the displacement δx (joint compression), collected in the vector $\boldsymbol{\xi} = [\alpha, \beta, \delta x]^{\mathrm{T}}$. The joint scheme is visible in Fig. 2a. The joint is actuated by three TSAs; we indicate with $\boldsymbol{\theta} = [\theta_1, \theta_2, \theta_3]^{\mathrm{T}}$, a vector collecting motor rotation angles. The forward kinematics analysis aims at defining the joint configuration obtained for a given set of motor rotation angles:

$$\boldsymbol{\xi} = \mathbf{f}_d(\boldsymbol{\theta}), \tag{1}$$

while the inverse kinematics analysis aims at defining the set of motor rotation angles needed to obtain a given joint configuration:

$$\boldsymbol{\theta} = \mathbf{f}_i(\boldsymbol{\xi}), \tag{2}$$

The system can be analyzed considering it as composed of two main parts: the soft joint structure and the TSAs. The corresponding models are connected each other by means of

another set of parameters, specifically TSA strokes, collected in the vector $\delta\mathbf{l} = [\delta l_1, \delta l_2, \delta l_3]^{\mathrm{T}}$. This assumption allows us to represent the direct kinematics relationship with two functions:

$$\boldsymbol{\xi} = \mathbf{f}_{d,J}(\delta\mathbf{l}), \tag{3}$$

$$\delta\mathbf{l} = \mathbf{f}_{d,A}(\boldsymbol{\theta}). \tag{4}$$

Similarly, inverse kinematics relationship can also be represented with two functions:

$$\boldsymbol{\theta} = \mathbf{f}_{i,A}(\delta\mathbf{l}), \tag{5}$$

$$\delta\mathbf{l} = \mathbf{f}_{i,J}(\boldsymbol{\xi}). \tag{6}$$

1) Joint direct and inverse kinematics: Let us consider that the joint connects the base reference frame $\mathcal{S}_0 = \{O_0, x_0, y_0, z_0\}$ with the frame $\mathcal{S}_1 = \{O_1, x_1, y_1, z_1\}$ on the proximal link. The reference frames are defined to be compliant with the Denavit-Hartenberg assumptions. The joint is actuated by three tendons, which we will denote as t_1, t_2, and t_3. Let us define three points A_1, A_2, and A_3, where the tendons leave the base, and three points B_1, B_2, and B_3, where the tendons reach the link. Let us assume that in the reference configuration, the planes containing A_i and B_i points are parallel and their distance is l_0, and that the tendons are parallel (i.e. the lines $\overline{A_iB_i}$ are parallel each other). For the sake of convenience, the reference frame $\mathcal{S}_0$, has the origin O_0 defined in the midpoint between A_1 and A_2, x_0 is perpendicular to the plane containing A_i points, z_0 passes through A_1 and A_2. The reference frame $\mathcal{S}_1$ is similarly defined on the link. Let us indicate with l_a the distance $l_a = \overline{A_1A_2} = \overline{B_1B_2}$ and with l_b the distance between A_3 and the midpoint between A_1 and A_2. Indicating with δl_1, δl_2, and δl_3 TSA strokes corresponding to tendons t_1, t_2, and t_3, respectively, joint configuration variables can be evaluated as follows:

$$\alpha = \arcsin\left(\frac{\delta l_1 - \delta l_2}{l_a}\right) \tag{7}$$

$$\beta = \arcsin\left(\frac{2\delta l_3 - (\delta l_1 + \delta l_2)}{2l_b}\right) \tag{8}$$

$$\delta x = \left(\frac{\delta l_1 + \delta l_2}{2}\right). \tag{9}$$

Eq. (7) — (9) define the function $\mathbf{f}_{d,J}$ introduced in eq. (3).

For a given joint configuration, the above introduced kinematics relationships can be inverted to find the corresponding tendon strokes. In particular, given the configuration variables $\boldsymbol{\xi}$, the corresponding homogeneous transformation matrix $\mathbf{T}_0^1(\boldsymbol{\xi})$ relating $\mathcal{S}_0$ and $\mathcal{S}_1$ can be evaluated with straightforward kinematics relationships. Indicating with $\mathbf{r}_{Ai}$ the coordinates of A_i points with respect to $\mathcal{S}_0$, and with $\mathbf{r}_{Bi}^1$ and $\mathbf{r}_{Bi}^0$ the coordinates of B_i points with respect to $\mathcal{S}_1$ and $\mathcal{S}_0$, respectively, it results:

$$\mathbf{r}_{Bi}^0 = \mathbf{T}_0^1(\boldsymbol{\xi})\mathbf{r}_{Bi}^1, \tag{10}$$

and

$$\delta l_i = \|\mathbf{r}_{Bi}^0 - \mathbf{r}_{Ai}^0\| - l_0 \tag{11}$$

Eq. (10) and (11) define the function $\mathbf{f}_{i,J}$ introduced in eq. (6).

2) TSA main kinematics and statics relationships: The mathematical models of TSA have been investigated from their introduction in robotic and mechatronic systems [11]. In this paper, we refer to one of the first and simplest models, proposed by Godler and Sonoda [12], which considers a TSA with $n_s = 2$ strings with radius r_s that on the side opposite to the motor are attached to the load at a distance $2A$. In the specific example presented in this work, $A = r_s$. Let us define l as the distance between the motor shaft and the end of the joint, where the strings are fixed. Its reference value, when the strings are untwisted, is l_{t0}. When the actuator is unloaded and untwisted, string length is given by $l_{0s} = \sqrt{(l_{t0}^2 + A^2)}$. When the i-th joint motor rotates with an angle θ_i, the pair of strings coils into a helix with radius $r_0 = r_s$, resulting in a contraction δl_i equal to:

$$\delta l_i = l_{t0} - \sqrt{l_{0s}^2 - (A + r_s\theta_i)^2}. \tag{12}$$

Eq. (12), applied to the three joint motors, represents the direct kinematic relationship $\mathbf{f}_{d,A}$ introduced in eq. (4). Eq. (12) can be inverted to find the actuator rotation angle θ_i needed to produce a TSA contraction δl_i:

$$\theta_i = \frac{1}{r}\left(\sqrt{A^2 + \delta l_i(l_0 - \delta l)} - A\right) \tag{13}$$

Eq. (13) defines the second part of the inverse kinematics relationship $\mathbf{f}_{i,A}$ introduced in eq. (5).

TSAs represent a non-linear rotation-to-translation mechanical transmission in which the maximum stroke depends on system properties. In particular, the so-called overtwisting phenomenon appears if the rotation angle exceeds a limit value θ_{max}. From the analysis of helix main properties, the helix angle φ can be calculated as:

$$\varphi_i = \arcsin\left(\frac{\sqrt{l_{0s}^2 - (A + \theta_i r_s)^2}}{l_{0s}}\right). \tag{14}$$

It is worth noticing that the minimum value of the helix angle φ_{min} is obtained when the helix coils are in contact with each other. The maximum actuator rotation angle θ_{max} that can be applied to prevent overtwist is:

$$\theta_{max} = \frac{\pi l_{0s} - A\sqrt{\pi^2 + 4}}{r_s\sqrt{\pi^2 + 4}}. \tag{15}$$

The maximum contraction ratio ρ_{max} that can be obtained from the TSA before overtwisting occurs is:

$$\rho_{max} = \frac{\delta l(\theta_{max})}{l_0} = \frac{l_0 - \sqrt{l_{0s}^2 - (A + r_s\theta)^2)}}{l_0}. \tag{16}$$

The above introduced relationships can be further investigated to analyze the differential kinematics and statics problem. In particular, by differentiating the relationship in eq. (12) we can evaluate the TSA transmission ratio η:

$$\eta = \frac{v}{\omega} = \frac{r_s(A + r_s\theta)}{\sqrt{l_{0s}^2 - (A + r_s\theta)^2}}, \tag{17}$$

where v is the TSA translation velocity while ω is the actuator rotation speed. Assuming 100% mechanical efficiency, the right-hand term in eq. (17) also expresses the

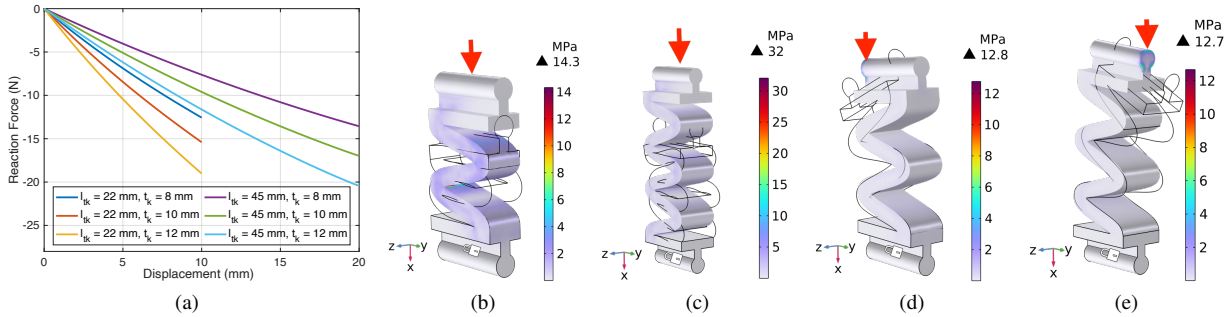

(a) (b) (c) (d) (e)

Fig. 3: Results of the 3-DoF joint characterization based on FEM analysis. (a) Compression test results in terms of reaction force under the prescribed displacement, as illustrated in (b) and (c), evaluated over the range $[0 : 0.1 : 10]$ mm for the joint with $l_{th} = 22.5$ mm and over $[0 : 0.1 : 20]$ mm for $l_{th} = 45$ mm, both with $t_k \in \{8, 10, 12\}$ mm. (b) and (c) show the corresponding stress distributions under a prescribed displacement along the x-axis of 10 mm for the joint with $l_{th} = 22.5$ mm and $t_k = 8$ mm, and of 20 mm for the joint with $l_{th} = 45$ mm and $t_k = 12$ mm, respectively. Lateral bending results are reported in (d) and (e), with a prescribed displacement of 15 mm applied to the left for a joint with $l_{th} = 30$ mm and $t_k = 10$ mm (d), and to the right for a joint with $l_{th} = 37.5$ mm and $t_k = 10$ mm (e). The red arrow indicates the location of the applied prescribed displacement, the padlock represents the fixed constraint of the joint, and the transparent wave frame illustrates the actual deformation.

ratio between the motor torque τ_i and the TSA pulling force F_z in quasistatic conditions.

Fig. 2b graphically shows the results of the kinematics and statics analysis of a TSA with $r_s = 0.3$ mm, and l_0 varying in the range $40-50$ mm. Specifically, in the figure the nonlinear transmission relationship between rotation angle θ_i and TSA stroke δl_i and the force that can be applied considering that the motor can apply a maximum torque $\tau_t = 0.228Nm$.

C. Preliminary Study Through Numerical Simulation

A structural analysis was conducted to estimate the force required to compress the 3-DoF soft joint and to verify whether the selected TSAs could provide sufficient actuation to control its compression, stiffness, and degrees of freedom. The study, based on the Finite Element Method (FEM), was performed using COMSOL Multiphysics® software. The material used for all modules was the Thermoplastic polyurethane (TPU) with shore hardness 95A, modeled with a nonlinear hyperelastic Mooney-Rivlin formulation.

In particular, the CAD model described above has been used. A series of analyses was then conducted on the compliant joint modules with the minimum and maximum lengths, i.e. $l_{th} \in \{22.5, 45\}$ mm and $t_k \in \{8, 10, 12\}$ mm. The analysis involved evaluating the reaction force corresponding to the maximum prescribed displacement defined by the module geometry. For joints with $l_{th} = 22.5$ mm, displacements in the range $[0 : 0.1 : 10]$ mm were applied, while for joints with $l_{th} = 45$ mm, the applied displacement range was $[0 : 0.1 : 20]$ mm. The results were compared with those obtained from the TSA model.

Fig. 3a shows that the reaction forces are within the range reproducible by the TSA. Fig. 3b and Fig. 3c show a representative set of results in terms of stress distribution: the transparent frame highlights the actual joint compression, the red arrow indicates the surface where the prescribed displacement was applied, and the white padlocks represent the constrained regions in the model. The results confirm that the applied displacement, simulating the action of the TSA, produces joint compression without undesired bending or buckling effects.

Fig. 3d and Fig. 3e present the FEM results in terms of stress for the samples with l_{th} = 30 mm, t_k = 10 mm and l_{th} = 37.5 mm, t_k = 12 mm. In this case, the focus was on evaluating lateral bending: leftward in Fig. 3d and rightward in Fig. 3e, under an applied displacement of 10 mm. Again, the red arrow indicates the imposed displacement surface, while the white padlocks indicate the constrained regions of the modules.

It is worth noting that the maximum equivalent stress sustainable by standard TPU is about 50 MPa. Results show that, in all case studies, the compliant structure is strong enough to withstand the simulated prescribe displacements conditions.

III. Characterization of the Joint

A. Experimental Setups

In this section, we experimentally evaluated the frontal and lateral joint stiffness by controlling the twisted string actuator. In these experiments, we have tested the joint for different lengths $l_{th} \in \{22.5, 30, 37.5, 45\}$ mm and thickness $t_k \in \{8, 10, 12\}$ mm, while keeping the distance between the ridges constant. The experimental setup is shown in Fig. 4. It consists of a test rig and an Acrylonitrile Butadiene Styrene (ABS) structure that houses the joint and the actuation system, which comprises two TSAs. Each TSA includes two polyethylene Dyneema® fiber cables (Japan) with a diameter of 0.6 mm, each capable of sustaining loads up to 450 N, anchored to a Dynamixel XL330-M077-T motor. Each motor provides a stall torque of 0.228 Nm at 6.0 V and is controlled via an OpenRB-150 microcontroller. The TSAs are mounted on an ABS support, as shown in Fig. 4b, which is positioned 50 mm from the base of the joint. This placement ensures that the generated force remains within the range required to compress the wave structure, as illustrated in Fig. 2b and

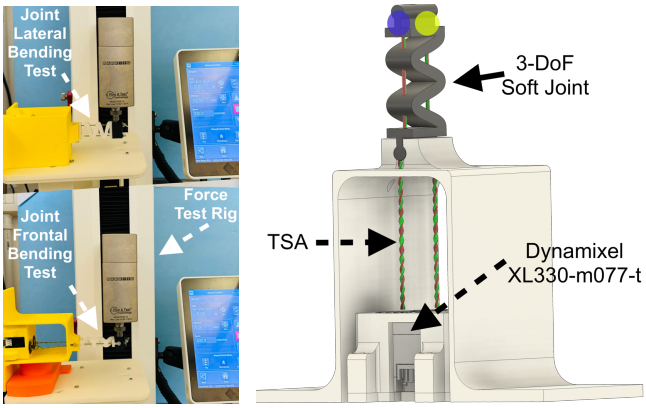

(a) (b)

Fig. 4: Experimental setup for joint characterization. (a) Lateral and frontal bending tests, performed on the top and bottom of the joint, respectively. (b) CAD of the structure housing the joint and TSA actuation system. The blue circle on the top of the joint indicates the area where the test rig applies a vertical force to measure lateral bending stiffness, while the yellow circle indicates the area where the force is applied to measure frontal bending stiffness.

Fig. 3a, while the compliant joint is mounted on top of the support.

Using this setup, tendons twists were adjusted by varying the turns of the motors, thereby compressing the compliant joint module. The frontal bending response of the soft joint was measured for different levels of twist using a vertical motorized force test rig (MARK-10 F305) equipped with an FS05-10 dynamometer (accuracy 0.02 N) and an EMP001-1 displacement measurement system. The joint support was fixed as visible on the lower part of Fig. 4a, while the joint was subjected to a vertical force applied to the yellow designated region in Fig. 4b, and the resulting deflection was recorded. Stiffness was determined as the slope of the force–displacement curve. Each measurement was repeated three times and the mean value was reported. The results are summarized in Table I. Stiffness is calculated in N/m. For the sake of readability of the table, we did not report the value of the standard deviation. However, the maximum value obtained among all tests was STD = 3.409 N/m. The procedure was similarly applied to assess lateral bending, with the joint rotated by 90° and fixed as shown in Fig. 4a top part. In this configuration, the force was applied to the region indicated in blue in Fig. 4b. The results are summarized in Table II. The maximum value obtained among all tests was STD = 4.183 N/m.

B. Results

The results reported in Table I and Table II provide a comprehensive characterization of the compliant joint's mechanical response and highlight the influence of geometry on stiffness. For a fixed thickness (t_k), both frontal and lateral stiffness decrease with increasing initial length. Shorter modules ($l_{th} = 22.5$ mm) consistently exhibit higher stiffness, while longer modules ($l_{th} = 45$ mm) are more compliant. This behavior aligns with fundamental structural principles, as compliance generally scales with the cube of the length in bending-dominated structures, reflecting the increased flexibility of longer wave-shaped modules.

Conversely, for a fixed length (l_{th}), stiffness increases with thickness. Thicker modules ($t_k = 12$ mm) sustain higher forces for a given displacement and exhibit a steeper force–displacement response compared to thinner modules ($t_k = 8$ mm). This trend is consistent with the expected dependence of bending stiffness on the effective cross-sectional area and moment of inertia of the compliant segment.

Moreover, for any given geometry (l_{th}, t_k), stiffness increases with compression. As the module shortens under tendons actuation, the slope of the force–displacement curve rises, reflecting the progressive resistance of the compliant wave structure.

The primary effects of length and thickness persist across the entire compression range. At any given number of actuator turns, the stiffness ranking follows $k(22.5\text{mm}, 12\text{mm}) > \ldots > k(45\text{mm}, 8\text{mm})$, with intermediate combinations falling in between. In practical terms, short-and-thick configurations deliver the highest stiffness, while long-and-thin configurations yield the lowest, providing designers with a predictable way to tune mechanical response.

These findings offer design guidelines for compliant robotic fingers and supernumerary limbs. To maximize stiffness, designers should reduce length and/or increase thickness; conversely, higher compliance can be achieved by increasing length and reducing thickness. Furthermore, tendons actuation provide a mechanism to fine-tune stiffness in real-time, enabling adaptive performance depending on task requirements. Overall, this parametric study establishes a clear relationship between geometry, actuation, and stiffness, forming a basis for the rational design of multi-DoF compliant joints in soft and wearable robotics.

IV. Application to a Wearable Robotic Supernumerary Finger

In the last decade, there has been a growing interest in wearable robotic supernumerary limbs, with a particular focus on supernumerary robotic arms and fingers [13]. The primary goal of these devices is to either compensate for impairments or augment human manipulation capabilities by adding additional limbs that can be seamlessly controlled by users.

Several supernumerary robotic fingers (SRF) have been proposed in the literature, sharing common design guidelines such as lightweight construction, adaptability, portability, and a compact form factor [10], [14]. Recently, Suthar *et al.* introduced a sixth-finger design that leverages TSA to achieve flexion/extension motion [15]. However, despite the variety of proposed models, only a few devices demonstrate the capability to perform abduction/adduction movements [16], which are crucial for enhancing dexterity and expanding

Length	*Width*	*Stiffness in function of the number of turns [N/m]*															
		0	1	2	3	4	5	6	7	8	9	10	11	12	13	14	15
22.5mm	8mm	143.395	148.367	154.844	162.297	173.072	188.436	207.451	231.067	257.454	289.728	331.337	377.655	438.786	508.947	613.462	761.659
	10mm	163.723	174.893	186.807	201.164	221.371	243.131	268.073	301.276	340.171	393.410	466.252	538.197	627.444	733.589	861.874	1042.990
	12mm	192.772	200.911	215.522	235.756	260.225	289.895	332.938	385.379	454.951	539.609	640.001	757.397	893.284	1038.49	1218.04	1475
30mm	8mm	100.323	103.966	108.395	115.002	123.362	132.155	144.052	160.415	177.408	197.97	223.309	256.42	301.56	361.224	442.872	567.277
	10mm	114.828	121.806	130.091	142.662	157.702	174.56	197.698	222.97	252.66	291.377	341.304	403.507	479.347	572.085	683.806	837.216
	12mm	134.922	140.681	152.774	168.787	188.507	220.59	245.533	289.785	348.338	409.026	482.082	573.507	683.867	804.832	967.757	1189.23
37.5mm	8mm	70.776	71.9096	75.045	79.94	85.267	91.624	100.454	108.25	119.8	133.603	151.226	175	206.548	248.13	307.759	390.137
	10mm	89.1323	92.1198	97.266	104.406	113.172	123.356	135.395	149.173	167.374	190.537	218.884	256.357	298.006	350.587	431.247	539.879
	12mm	114.894	116.337	121.885	128.82	137.195	147.145	165.624	185.14	209.011	239.143	281.623	329.724	396.496	478.647	571.631	718.111
45mm	8mm	53.333	54.343	56.058	58.471	61.133	65.145	71.238	79.106	89.537	100.552	113.226	127.911	143.402	161.176	182.727	213.406
	10mm	65.023	66.9231	70.0896	73.949	78	83.603	90.91	100.561	114.143	128.071	145.907	165	191.333	224.471	266.889	322.211
	12mm	80.745	81.857	83.695	87.868	94.263	102.879	114.117	127.505	142.842	160.162	182.831	207.162	238.649	272	319.898	378.182

TABLE I: Experimental frontal stiffness of the proposed compliant joint for varying widths, lengths and compression, highlighting the influence of geometric parameters on mechanical response.

Length	*Width*	*Stiffness in function of the number of turns [N/m]*															
		0	1	2	3	4	5	6	7	8	9	10	11	12	13	14	15
22.5mm	8mm	400.274	419.959	462.747	527.053	606.839	701.161	829.384	984.504	1157.14	1354.39	1521.54	1717.76	2027.75	2504.99	3112.43	4066.67
	10mm	480.866	504.3	566.814	676.667	832.495	1037.99	1282.67	1588.84	1936.64	2374.05	2896.83	3550.54	4372.06	5294.97	6281.13	7890.55
	12mm	582.428	615.209	713.708	850.747	1080.15	1355.07	1679.9	2197.56	2711.97	3446.95	4184.48	5207.21	6323.68	7595.94	9200.74	12318.1
30mm	8mm	256.416	277.392	309.86	352.358	399.322	448.068	525.024	604.74	735.974	865.078	1049.89	1277.97	1560.55	1904.37	2371.97	3186.2
	10mm	326.447	378.31	433.329	526.838	641.403	768.508	929.593	1103.33	1298.24	1545.62	1840.93	2266.83	2738.51	3427.06	4298.64	5535.34
	12mm	422.132	454.515	543.776	666.032	790.239	1012.9	1293.45	1592.7	1984.66	2425.5	3065.46	3600.53	4317.77	5222.66	6206.93	7728.85
37.5mm	8mm	189.155	205.385	225.45	250.812	269.966	309.747	360.555	419.52	510.278	622.565	734.998	863.885	1018.32	1257.4	1559.78	2056.67
	10mm	251.828	295.843	337.632	406.083	497.082	610.948	743.438	889.771	1035.53	1205.4	1442.39	1734.66	2087.56	2499.17	2970.93	3748.94
	12mm	332.6	371.751	451.751	552.507	666.389	773.231	939.027	1178.36	1452.84	1727.28	2059.92	2471.48	2937.99	3606.29	4589.44	6019.67
45mm	8mm	159.168	166.808	175.645	190.093	210.39	238.338	265.611	300.578	342.988	390.088	460.484	544.017	641.22	776.667	988.148	1408.32
	10mm	210.757	213.157	229.993	253.074	287.735	332.113	395.731	480.413	555.224	664.049	781.111	901.37	1084.18	1355	1745.96	2256.23
	12mm	263.968	271.207	290.969	316.844	356.432	431.072	504.39	614.233	758.112	920.379	1083.64	1331.75	1633.33	2129.55	2722.22	3616.67

TABLE II: Experimental lateral stiffness values of the proposed compliant joint measured for different combinations of module width, length and compression.

the manipulation workspace. Usually only flexion/extension capabilities are achieved with a tendon-driven actuation.

The joint presented in this work can potentially address these limitations by providing enhanced dexterity while maintaining low weight and a reduced form factor. To demonstrate its potential, we have developed a novel wearable SRF in which the proposed joint is integrated as the base joint. This design enables active abduction/adduction along with flexion/extension, while also allowing modulation of stiffness and effective joint length. These features significantly increase the mobility and dexterity of the SRF.

A. Device Explanation

The rendering of the developed device is shown in Fig. 5. The new SRF consists of five rigid phalanges, four 1-DoF compliant joints, and one 3-DoF compliant joint at the base. The 3-DoF soft joint was designed with t_k = 10 mm and a l_{th} = 30 mm, maintaining the same overall finger length as in [10], under the 3-DoF compliant joint compression. The joints are fabricated in TPU (Shore hardness 95A), while the phalanges and the forearm support are made of ABS. The electronic components and actuation unit are housed on the back of the forearm support.

The actuation unit comprises three TSAs: the two lateral TSAs control the 3-DoF compliant joint, while the central one drives finger flexion. Each TSA consists of two cables (polyethylene Dyneema fiber, Japan) with a diameter of 0.6

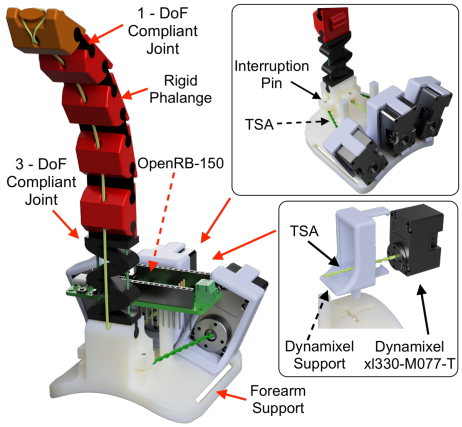

Fig. 5: The SRF with the proposed joint at the base allowing for flexion/extension and abduction/adduction.

mm, each capable of sustaining up to 450 N, and anchored to a Dynamixel XL330-M077-T motor mounted inside an ABS housing fixed to the forearm support, as visible in Fig. 5. The motors exploit the TSA principle to induce tendon contraction and are characterized by a lightweight and compact design, low-voltage operation, a stall torque of 0.228 Nm, and a maximum speed of 456 rev/min, making them highly suitable for TSA-based actuation. To ensure proper TSA functionality [17], the twisting action of the tendons (twisting zone) is mechanically constrained by an interruption pin

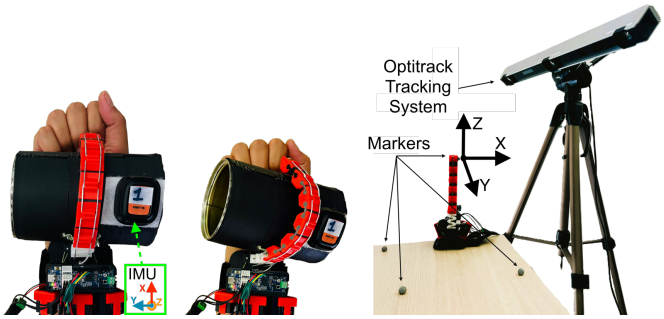

(a) (b) (c)

Fig. 6: (a) and (b) Dexterity test. The SRF equipped with the 3-DoF joint ($l_{th} = 45$ mm, $t_k = 10$ mm) is shown (a) grasping a cylindrical object with a diameter of 80 mm, and (b) tilting the same object. (c) Workspace experimental setup.

located at the base of the finger, as shown in Fig. 5. The twisting zone was designed with a length of 50 mm to enable effective compression of the wave-shaped joint, in accordance with the considerations discussed in Sec. II. The device is controlled by an OpenRB-150 board equipped with a 32-bit SAMD21 Cortex-M0 microcontroller and powered by an external supply. Communication is supported via USB or Bluetooth through the RN-42 module (Roving Networks Inc., US).

B. Experiments

The proposed SRF incorporates a compliant base joint that adds abduction/adduction and compression degrees of freedom to the existing flexion/extension axis, resulting in a 3-DoF motion capability. Experiments were conducted to evaluate finger dexterity, characterize the reachable workspace, and assess manipulation performance. Dexterity tests measured the achievable range of motion around the flexion/extension and abduction/adduction axes, while workspace characterization mapped the collision-free, constant-orientation reachable set of the fingertip in a fixed reference frame, summarizing coverage using volumetric and boundary metrics. Finally, the manipulation capabilities were demonstrated qualitatively through grasping of objects.

1) Dexterity test: The experimental arrangement visible in Fig. 6a and Fig. 6b positioned the SRF to grasp a cylindrical test object with a diameter of 80 mm. After establishing a stable grasp, the TSA at the compliant base joint was driven to elicit lateral abduction/adduction motions while maintaining the flexion/extension posture. An Inertial Measurement Units (IMU), Xsens Dot, was mounted on the object to record 3D orientation. Data were in offline recording mode at 120 Hz. The experiment was repeated by using two compliant wave joint, *i.e.* for $l_{th} \in \{30, 45\}$ mm and $t_k = 10$ mm, each of them five times.

Fig. 7 shows the results of a representative trial. The TSA pre-twist effectively modulated the lateral stiffness of the compliant base joint, enabling controlled object reorientation under load. Increasing the base-joint length systematically enhanced lateral rotation (manipulability angle), with longer

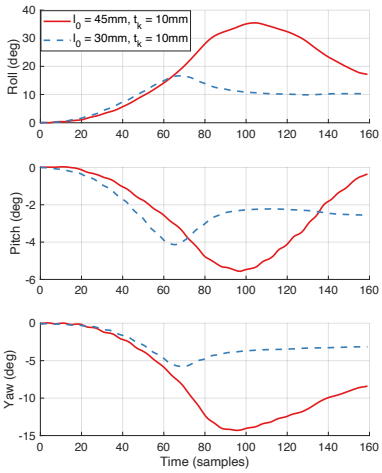

Fig. 7: Results of a representative dexterity test trial in terms of roll, pitch, and yaw angles measured by the IMU. The red line corresponds to the robotic finger equipped with the joint ($l_{th} = 45$ mm, $t_k = 10$ mm), while the blue dotted line refers to the joint with ($l_{th} = 30$ mm, $t_k = 10$ mm).

configurations achieving larger abduction/adduction excursions. Specifically, for $l_{th} = 45$ mm, the observed rotations were Roll $= 35.45° \pm 2.12$, Pitch $= -5.53° \pm 1.42$, and Yaw $= -14.31° \pm 1.58$, while for $l_{th} = 30$ mm, the rotations were Roll $= 16.67° \pm 2.04$, Pitch $= -4.15° \pm 1.08$, and Yaw $= -5.72° \pm 1.54$. These results highlight that longer base-joint configurations provide greater lateral mobility, allowing the supernumerary finger to achieve enhanced dexterity during object manipulation.

2) Workspace test: The workspace of the proposed SRF was evaluated using a multi-camera optical motion-capture system, V120 Trio 6-DoF object tracking (OptiTrack Systems, UK), providing a positional accuracy of ± 0.2 mm. A single reflective marker was attached to the fingertip, allowing continuous 3D tracking of its position in the global capture frame. The experimental setup is illustrated in Fig. 6c.

For the experiments, the robotic finger was positioned on a flat table, providing a stable reference plane. The device executed flexion/extension motions such that the fingertip descended until it came into contact with the table surface, simulating realistic functional motion constraints. In addition, abduction/adduction motions were performed to capture lateral mobility. Each motion type was repeated across two base-joint lengths i.e., for $l_{th} \in \{22.5, 45\}$ mm and $t_k = 10$ mm, to assess the influence of geometric parameters on the reachable workspace.

For each trial, fingertip trajectories data were collected at a frequency of 100 Hz and processed in MATLAB. The recorded data allowed reconstruction of the full 3D workspace, including maximum reach and orientation range of the fingertip. Representative visualizations of the resulting workspaces are shown in Fig. 8.

With the new compliant base-joint, the workspace reachable with the fingertip is increased enabling a broader set

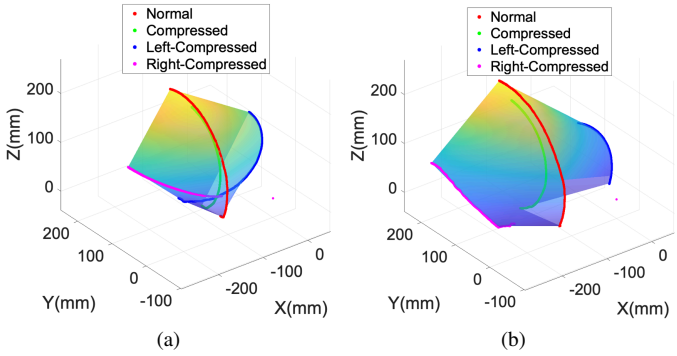

Fig. 8: Workspace test. (a) Workspace of the SRF with the 3-DoF compliant joint with $l_{th} = 22.5$ mm, $t_k = 10$ mm and total volume $V = 0.003$ m^3. (b) Workspace of the robotic finger with $l_{th} = 45$ mm, $t_k = 10$ mm and $V = 0.006$ m^3.

Fig. 9: Grasping of spherical and irregularly shaped objects with the 3-DoF compliant joint ($l_{th} = 30$ mm, $t_k = 10$ mm). (a) grasp of a sphere. (b) sphere tilted to the left. (c) grasp of a bottle. (d) the bottle tilted to the right.

of possible grasps. This qualitative trend is consistently observed across the tested joint lengths: larger lengths increase lateral reach, thus increasing overall workspace volume as in Fig. 8b, compared to smaller workspace volume Fig. 8a.

3) Manipulation test: We evaluated the ability of the robotic finger to manipulate objects of different shapes. The test consisted of performing a stable grasp on the object, followed by a controlled displacement to assess its manipulability. Objects with cylindrical, spherical, and irregular geometries were used, including a ball, a box, a jar and a small airplane toy. Fig. 9 illustrates the capability of the device to grasp and manipulate a ball and a bottle, while the accompanying video demonstrates the manipulation of the other objects.

V. Conclusion

This paper presented a novel parametric wave-structured 3-DoF compliant joint with tunable stiffness, designed to enhance dexterity while maintaining a compact and lightweight structure. The proposed design integrates TSA to enable active modulation of stiffness and joint mobility.

Analytical modeling, numerical simulations, and experimental characterization validated the joint's mechanical properties and confirmed its capability to achieve a wide range of stiffness values and motion profiles. Integration of the joint into a wearable SRF demonstrated a significant increase in workspace and dexterity, highlighting its potential as a versatile component for assistive and augmentative systems.

Future work will focus on developing advanced control strategies to fully exploit the joint's multi-DoF capabilities, optimizing its geometry for specific manipulation tasks, and evaluating its usability and ergonomics in real-world scenarios, including clinical and industrial applications.

References

[1] W. Park, S. Seo, and J. Bae, "A hybrid gripper with soft material and rigid structures," *IEEE Robotics and Automation Letters*, vol. 4, no. 1, pp. 65–72, 2018.

[2] G. Salvietti, Z. Iqbal, I. Hussain, D. Prattichizzo, and M. Malvezzi, "The co-gripper: a wireless cooperative gripper for safe human robot interaction," in *2018 IEEE/RSJ International Conference on Intelligent Robots and Systems (IROS)*. IEEE, 2018, pp. 4576–4581.

[3] R. Ma and A. Dollar, "Yale openhand project: Optimizing open-source hand designs for ease of fabrication and adoption," *IEEE Robotics & Automation Magazine*, vol. 24, no. 1, pp. 32–40, 2017.

[4] I. Hussain, G. Salvietti, M. Malvezzi, and D. Prattichizzo, "On the role of stiffness design for fingertip trajectories of underactuated modular soft hands," in *2017 IEEE International Conference on Robotics and Automation (ICRA)*. IEEE, 2017, pp. 3096–3101.

[5] J.-y. Nagase, S. Wakimoto, T. Satoh, N. Saga, and K. Suzumori, "Design of a variable-stiffness robotic hand using pneumatic soft rubber actuators," *Smart Materials and Structures*, vol. 20, no. 10, p. 105015, 2011.

[6] M. Grebenstein, M. Chalon, W. Friedl, S. Haddadin, T. Wimböck, G. Hirzinger, and R. Siegwart, "The hand of the dlr hand arm system: Designed for interaction," *The International Journal of Robotics Research*, vol. 31, no. 13, pp. 1531–1555, 2012.

[7] M. Dragusanu, G. M. Achilli, M. C. Valigi, D. Prattichizzo, M. Malvezzi, and G. Salvietti, "The wavejoints: a novel methodology to design soft-rigid grippers made by monolithic 3d printed fingers with adjustable joint stiffness," in *2022 international conference on robotics and automation (ICRA)*. IEEE, 2022, pp. 6173–6179.

[8] M. Dragusanu, D. Troisi, D. Prattichizzo, and M. Malvezzi, "Compliant finger joint with controlled variable stiffness based on twisted strings actuation," in *2023 IEEE International Conference on Robotics and Automation (ICRA)*, 2023, pp. 7378–7384.

[9] P. Mansueto, M. Dragusanu, A. Saeed, M. Malvezzi, M. Lapucci, and G. Salvietti, "Optimization-driven design of monolithic soft-rigid grippers," *Soft Robotics*, 2025.

[10] G. Salvietti, I. Hussain, D. Cioncoloni, S. Taddei, S. Rossi, and D. Prattichizzo, "Compensating hand function in chronic stroke patients through the robotic sixth finger," *IEEE TNRSE*, vol. 25, no. 2, pp. 142–150, 2016.

[11] M. Malvezzi, B. Suthar, and M. Dragusanu, "Twisted string actuators: Comprehensive review on modeling, design innovations, application advances, and future challenges," *Measurement*, vol. 257, p. 118824, 2026.

[12] I. Godler and T. Sonoda, "A five fingered robotic hand prototype by using twist drive," in *ISR 2010 (41st International Symposium on Robotics) and ROBOTIK 2010 (6th German Conference on Robotics)*. VDE, 2010, pp. 1–6.

[13] D. Prattichizzo, M. Pozzi, T. L. Baldi, M. Malvezzi, I. Hussain, S. Rossi, and G. Salvietti, "Human augmentation by wearable supernumerary robotic limbs: review and perspectives," *Progress in Biomedical Engineering*, vol. 3, no. 4, p. 042005, 2021.

[14] I. Hussain, G. Salvietti, G. Spagnoletti, M. Malvezzi, D. Cioncoloni, S. Rossi, and D. Prattichizzo, "A soft supernumerary robotic finger and mobile arm support for grasping compensation and hemiparetic upper limb rehabilitation," *Robotics and Autonomous Systems*, vol. 93, pp. 1–12, 2017.

[15] B. Suthar, M. I. Awad, L. Seneviratne, Y. Zweiri, and I. Hussain, "Design of robotic finger using twisted string actuator with modular passive return rotational joints to achieve high grasping force: Application to wearable sixth finger," *Mechatronics*, vol. 99, p. 103157, 2024.

[16] P. Kieliba, D. Clode, R. O. Maimon-Mor, and T. R. Makin, "Robotic hand augmentation drives changes in neural body representation," *Science robotics*, vol. 6, no. 54, p. eabd7935, 2021.

[17] M. Dragusanu, D. Troisi, B. Suthar, I. Hussain, D. Prattichizzo, and M. Malvezzi, "Mglove-ts: A modular soft glove based on twisted string actuators and flexible structures," *Mechatronics*, vol. 98, p. 103141, 2024.